Magnetically propelled chained nanocomposites for biologically relevant media exploration

Miguel A. Ramos-Docampo [a,b], Pablo Hurtado [c], Ana B. Dávila-Ibáñez [c], Roberto Piñeiro [c], Mónica L. Fanarraga [d], Verónica Salgueiriño [a,b]

[a] Departamento de Física Aplicada, Universidade de Vigo, 36310 Vigo, Spain
[b] CINBIO, Universidade de Vigo, 36310 Vigo, Spain
[c] Roche-Chus Joint Unit, Translational Medical Oncology Group, Oncomet, Health Research Institute of Santiago de Compostela, 15706 Santiago de Compostela, Spain
[d] Nanomedicine Group, Universidad de Cantabria-IDIVAL, 39011 Santander, Spain

GRAPHICAL ABSTRACT
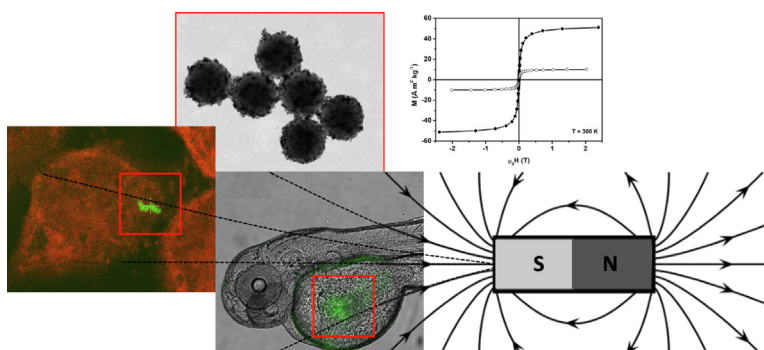
ARTICLE INFO

ABSTRACT

Elongated nanostructures to be remotely and magnetically propelled in biologically relevant media, have gained attention as offering themselves as effective tools or carriers in theragnostics applications. However, the magnetic actuation associated remains challenging due to the lack of mechanical information in the media of interest, taking into account biophysical or biomedical purposes. In this study, we detail the magnetic actuation of magnetically propelled chained nanocomposites considering their dynamics, in which their velocity can be modulated in terms of the viscosity of the medium considered, given a magnetic field gradient. Simpler cases of distilled water, a water/glycerol mixture and a fluid made of cell extracts (imitating the cytosol of cells) of known viscosity are the basis experiments for the study of more complex media inside HeLa cells, murine NIH-3T3 fibroblasts and zebrafish larvae, offering the mechanical information required. The experimental results indicate that the magnetically propelled performance of the chained nanostructures can be precisely controlled in potentially changing scenarios, where drug and heat delivery, magnetic separation, or microfluidic technologies are demanded, using a magnetic field gradient and providing good estimations of the dynamical parameters involved.

E-mail address: vsalgue@uvigo.es (V. Salgueiriño)

1. Introduction

Controlled navigation in different regions of a body shows a huge potential when it comes to considering biodevices for minimally invasive interventions or medical treatments [1]. However, the different mechanisms for such control, such as power sourcing, precise actuation, swarm control, *in vivo* imaging, real-time motion tracking, low cytotoxicity, diagnosis treatment integration, and biodegradation are yet to be satisfactorily resolved before clinical translation. In this context, the magnetic manipulation at a distance offers a profuse option regarding these requirements: [2,3] the use of an external magnetic force as power sourcing [4,5] and for precise actuation [6,8], possible swarm control given coordinated dipolar interactions to be established [9], convenient relaxation times to be finely tuned for magnetic resonance imaging [10], and the consequent possibility of real-time motion tracking [11,12]. As such, the presence of the magnetic field gradient for a controlled magnetic manipulation implies a "magnetic" drag force and the consequent acceleration, overcoming the hydrodynamic (viscous) drag force [13], for the navigating systems to move cooperatively where required. This cooperation stems from the fact that while the magnetic force pulls the nanostructures, a simultaneous magnetic torque causes such structures to rapidly align forming chains, increasing the total magnetic moment and consequently the magnetic force acting on them.

In this context, analyzing and tracking the magnetic manipulation of individual or assemblies of nanoparticles is usually simplified considering them under the influence of Stokes drag and the magnetic force alone, with no fluid stream but just the Brownian diffusion. However, besides fluid stream, increasing the complexity of the media where these nanostructures are dispersed implies interactions and collisions that cause them to undergo a diffusive motion which is much greater than the standard Brownian motion [14]. In fact, most of the micro- and nano-swimmers and motors, when administered *via* common routes, face high viscosity biological media and yet, performance has only been proved in very diluted dispersions [15,16]. Accordingly, though reliable, these studies are lacking comprehensive depth to deal with the complexity of biologically relevant media.

When it comes to consider micro and nanoscale dynamics, inertia is unimportant and the Reynolds number is small, and therefore, there are some flow singularities and kinematic requirements for net translation. The Reynolds number is a dimensionless quantity that qualitatively captures the characteristics of the flow regime. For example for a low Reynolds number flow, viscous forces dominate in the fluid and the fluid transport is ruled by viscous diffusion [17,18]. Therefore, a major challenge in this field of biophysics involves mechanical principles of locomotion with a low Reynolds number at the small scales, that is, tens of micrometers and below, where while inertia plays little role, viscous damping is paramount. This combination strongly influences the velocity relative to the carrier fluid attained by magnetic nano/microstructures, through the magnetophoretic mobility [13,19]. Consequently, to achieve their effective manipulation considering the magnetic strategy for steering and directing the motion, cases of viscosity-dependent complex motility taking place in biologically relevant media such as in the cell interior (the cytosol) and in other living systems should be further detailed. For example, zebrafish larvae have been demonstrated as a very convenient correlative *in vivo* vertebrate animal model for addressing nanotechnology experiments [20,21], offering biological complexities that involve not only the dynamics of interest but also events of multicellular organisms that individual cells and cell cultures fail to provide [22,23].

This magnetically-induced motility of active Brownian nanocomposites to work as microrobots is driven by an externally oriented magnetic field gradient. To describe and control the dynamic features of this effect to be used with biodevices for minimally invasive interventions [24], we have proceeded with an experimental framework on which the complexity of the medium increases, to prove its influence in the arrangement of magnetic nanocomposites in chains, and the average velocity reached. These results are used to verify the effective magnetic manipulation using mean-square displacements that can differentiate this magnetic propulsion from the Brownian motion [16,25], finding that viscosity affects both the length of the magnetic chains formed, and the magnetophoretic ability they become endorsed with. We validate therefore the magnetic manipulation of chained nanocomposites: (a) extracting information regarding key dynamical parameters (viscosity-dependent diffusion coefficient or velocity) in the explored media, and (b) offering a better understanding of the magnetophoretic behavior exhibited, when immersed in cells or organs inside living systems.

2. Materials and methods

2.1. Chemicals

Iron(II) sulfate heptahydrate ($FeSO_4 \cdot 7H_2O$), and hydrochloric acid (HCl, 37 wt%), poly(allylamine hydrochloride) (PAH, 17500 MW), poly(fluorescein isothiocyanate allylamine hydrochloride) (PAH-FITC, grafting ratio 50:1), poly(sodium-4-styrenesulfate) (PSS, 70,000 MW), sodium chloride (NaCl, >99.5%), glycerol (99.5%), N –Phenylthiourea (PTU), and tricaine were purchased from Sigma-Aldrich. Ammonium hydroxide solution (NH_4OH, 29 wt% NH_3), and iron(III) chloride hexahydrate ($FeCl_3 \cdot 6H_2O$, 97%) were provided by Fluka. Polystyrene spheres (PS, 500 ± 50 nm, 100 mg mL^{-1}) were available from Ikerlat Polymers. Milli-Q water (18.2 MΩ cm resistance). All chemicals were used without any further purification or treatment. Murine livers were mechanically dissociated in phosphate-buffered saline solution (PBS) pH 7.4 for the preparation of cell extracts. Cells/DNA were lysed using a probe ultrasonicator and the cellular extracts were cleared using centrifugation at 20.000 g at 4 °C for 30 min.

2.2. Synthesis of iron oxide (Fe_3O_4/γ-Fe_2O_3) nanoparticles

The synthesis of iron oxide nanoparticles was carried out following the Massart's method. [26] Accordingly, 1 mL of a (2 M) $FeSO_4 \cdot 7H_2O$ aqueous solution (dissolved in a solution of (2 M) HCl) and 4 mL of a (1 M) $FeCl_3 \cdot 6H_2O$ aqueous solution were prepared. Both solutions were rapidly poured into 50 mL of a (0.34 M) NH_4OH (29 wt%) solution under mechanical, vigorous stirring. The stirring was maintained for 30 min and finally, the nanoparticles were allowed to sediment. After 5 washing (water) cycles of sedimentation and decantation of the supernatant, the magnetite nanoparticles were dispersed in 50 mL in ultrapure water.

2.3. Synthesis of PS@IO nanocomposites

To produce the nanocomposites, 130 μL of polystyrene spheres (PS) (100 mg mL^{-1}) (of 500 nm in diameter) were diluted up to 2 mL in ultrapure water. 15 mL of PAH (1 mg mL^{-1} in 0.5 M NaCl solution) were added subsequently under soft ultrasonication and allowed to orbital-shake for 1 h. The excess of PAH was removed by 3 cycles of centrifugation in ultrapure water. Then, 15 mL of PSS (1 mg mL^{-1} in 0.5 M NaCl solution) were added,

and the procedure was repeated up to complete 4 layers of alternated polyelectrolytes, following a layer-by-layer protocol. The PS spheres with four layers of polyelectrolytes were dispersed in 10 mL of ultrapure water. Finally, 160 µL of the freshly prepared solution of iron oxide nanoparticles were diluted up to 5 mL in ultrapure water and mixed with the polyelectrolyte-coated PS solution. The mixture was shaken for 1 h. Afterwards, the colloids were washed by 3 cycles of centrifugation. Additionally, to render the nanocomposites fluorescent, a bilayer of PSS and PAH-FITC (poly(sodium-4-styrenesulfate and (poly(fluorescein isothiocyanate allylamine hydrochloride, respectively) was added, following the previous procedure, having the final colloids redispersed in 2 mL of ultrapure water. For the mobility experiments in zebrafish, 3.5 µm polystyrene spheres (10 mg mL^{-1}) were used instead, to better visualize the assemblies inside.

2.4. Chained swimmers formation and magnetic guidance

The colloids were dispersed in the medium of study, at a concentration of 1 mg/mL. The dispersion was transferred into microscope slices that were *time-lapse* imaged using a Nikon A1R scanning confocal microscope. The colloids were allowed to sediment within 2 min. Then, the movies were recorded in the absence and presence of a 15 mT magnetic field. Movies were recorded at 200 ms for 2–5 min. The trajectories of each individual nanostructure or linear assembly were tracked using the tracking option from NISS Elements software. The trajectories were extracted and imported into a data processing software, where the mean-squared displacement analysis was performed using a protocol published elsewhere [25].

2.5. Materials characterization

X-ray diffraction (XRD) patterns from powdered samples were collected using a Panalytical X'Pert Pro diffractometer (Cu K$_\alpha$ radiation, Bragg-Brentano θ–2θ geometry) in the 2θ angular range of 10–80° using a continuous scan mode (step = 0.026°, 4 s per step). The data collected were refined using the Le Bail method using Rietica software. Transmission electron microscopy (TEM) images were performed on a JEOL JEM1010 instrument operating at an acceleration voltage of 100 kV. Samples for TEM analysis were prepared by dropping a diluted suspension of the nanoparticles onto an ultrathin carbon-coated copper grid. Raman spectra were collected with a Renishaw in Via Reflex Raman Microscope. Experiments were conducted at room temperature using a 532 nm laser excitation wavelength. The laser beam was focused on the sample by a 20× objective, with a numerical aperture (NA) value of 0.40. Magnetic measurements were performed using the vibrating sample magnetometer (VSM) option in a Physical Property Measurement System (PPMS) from Quantum Design. Hysteresis loops were measured at 300 K up to an external field of 2 T in powdered samples. The temperature-dependent magnetization in zero-field-cooling (ZFC) and field-cooling (FC-10 mT) conditions was recorded applying a 10 mT magnetic field in the 10–320 K temperature range. The LbL (layer-by-layer) self-assembly was confirmed by ζ-potential measurements, using a Zetasizer Nanoseries.

2.6. Cell culture and confocal microscopy imaging

Particles were serum-functionalized (10 µg/mL) in the medium of cultured human epithelial cells (HeLa) or murine NIH-3 T3 fibroblasts, grown on the surface of culture dishes [27]. For high-resolution confocal microscopy observation, some of the cultures were placed onto or under a magnet for the indicated times. Cells were fixed with 4% paraformaldehyde and stained with ethidium bromide and Hoechst. A Nikon A1R confocal microscopy equipped with a Plan Apochromatic 100 x oil 1.45 NA objective was used. Live cell imaging and intracellular particle speed quantification were performed using the tracking model of the NIS-Elements Advanced Research software.

2.7. Zebrafish experiments

Zebrafish (*Danio rerio*) embryos were generated by natural mating of adult fish. Embryos were incubated with PTU (N –Phenylthiourea), at a 0.003% w/v concentration to avoid surface pigmentation, and maintained at 28 °C. For the mobility assays, 2-days post-fertilization (dpf) zebrafish embryos were dechorionized, anesthetized with 0.003% tricaine w/v in E3 water and positioned on a 10 cm Petri dish coated with 1.5% agarose. Fluorescent polystyrene spheres (10 mg mL^{-1}) of 3.5 µm coated with a bilayer of poly (fluorescein isothiocyante allylamine hydrochloride (PAH-FITC) and poly (sodium-4-styrenesulfate) (PSS) were used in the experiments. For microinjection, the nanocomposites suspension was loaded in borosilicate glass capillary needles (1 mm O.D. × 0.58 mm I.D, Harvard Apparatus) and injected into the yolk sac using a micromanipulator and an IM 300 microinjector (Narishige) with an output pressure of 1 psi and 0.3 ms injection time. Immediately after injection, embryos were photographed with a fluorescent microscope DMi8 (Leica) to determine the presence and location of the nanocomposites and placed at 28 °C for 45 min. Embryos were incubated in the presence or absence of an external magnetic field and, after 45 min, embryos from both groups were photographed again. The movement of nanocomposites inside the yolk sac was analyzed with the software ImageJ Fiji, measuring the distance travelled in the direction of the magnetic field between initial point (moment of injection) and final point (45 min after injection), taking as reference for the measurements the closet part of the nanocomposites suspension to the magnet at each time point. For each condition, data are representative of at least four independent experiments, with at least 15 embryos per group.

3. Results and discussion

3.1. Nanoparticles and nanocomposites

The synthesis of the magnetic nanoparticles was carried out using the Massart method, [26] which consists of the instantaneous co-precipitation of Fe^{2+} and Fe^{3+} ions (catalyzed by alkali media) to form an iron oxide phase, and endorses the nanoparticles with enough charge at the surface for their subsequent polyelectrolyte-assisted deposition onto polystyrene (PS) spheres. Fig. 1a includes a representative transmission electron microscopy (TEM) image of the nanoparticles (the size distribution analysis is shown in Fig. S1, in the supplementary data (SD), indicating an average diameter of 8.7*/1.3 nm (log-normal fit) [28]. Fig. 1b shows the X-ray diffraction (XRD) pattern, confirming the spinel crystalline structure of the iron oxide obtained. For a more detailed assessment, the XRD pattern was analyzed using the LeBail refinement, permitting the assignment of peaks to the cubic spinel structure (*Fd*-3 *m* space group). The cell parameter obtained using the LeBail refinement (Rietica software) for the nanocrystals is 0.8351 nm, which is close to the one reported for pure bulk magnetite (*a* = 0.8396 nm). Raman spectroscopy was also employed for the structural study of the magnetic nanoparticles, permitting the differentiation between magnetite and maghemite [29]. Fig. 1c includes the Raman spectra collected at room temperature, using a 633 nm excitation wavelength and keeping the laser power below 1 mW, to avoid further oxidation of the sample. According to
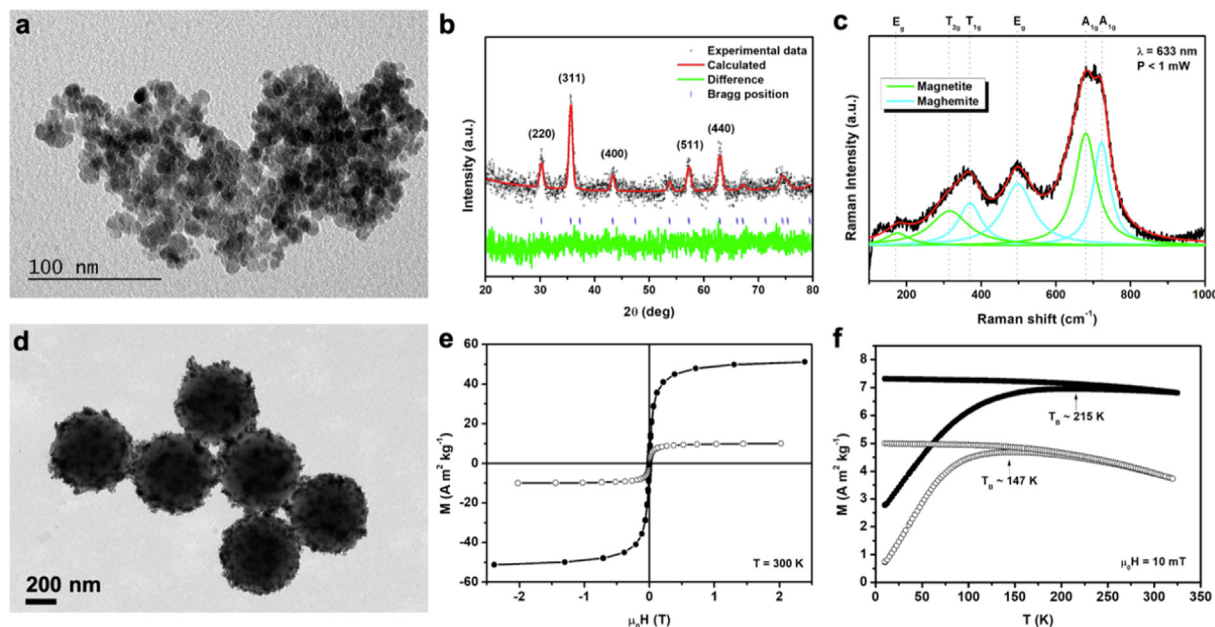
Fig. 1. TEM image (a), XRD pattern with LeBail refinement (b), and Raman spectra (c) of the iron oxide nanoparticles; TEM image of the PS@IO nanocomposites (d); and magnetic characterization of the samples in terms of magnetization *versus* magnetic field (e) and *versus* temperature (f) for the nanoparticles (solid symbols) and the nanocomposites (hollow symbols).

group theory, the spinel structure presents five Raman active modes, namely A_{1g}, E_g, and 3 T_{2g}, of which the A_{1g} centered at 680 cm^{-1}, the E_g at 314 cm^{-1} and one of the T_{2g} at 175 cm^{-1}, were registered. The deconvolution of these bands using a Lorentzian fitting renders visible the expected vibrational modes, indicated in green in Fig. 1c, confirming the presence of magnetite (Fe$_3$O$_4$). However, the three additional bands (in blue) centered at 370 cm^{-1}, 496 cm^{-1} and 726 cm^{-1}, indicate the presence of the maghemite phase (γ-Fe$_2$O$_3$) as well [30]. Summarizing this part, using the Massart method, we have obtained iron oxide (Fe$_3$O$_4$/ γ-Fe$_2$O$_3$) nanoparticles, which as being partially oxidized at the surface, they are passivated and endorsed with a positively charged surface, as indicated by the ζ-potential value registered ($\zeta \sim$ +20 mV).

For the fabrication of the magnetic nanocomposites, these iron oxide nanoparticles were deposited onto PS beads. These spherical substrates, with an average diameter of 500 ± 50 nm, were first functionalized by the alternated adsorption of oppositely charged polyelectrolytes, poly(allylamine hydrochloride (PAH) and poly(-sodium sulfonate) (PSS), attaining ζ-potential values of +20 and −35 mV, respectively [31]. Fig. 1d shows a representative TEM image of these iron oxide-coated polystyrene spheres (PS@IO) nanocomposites with a core@shell morphology, with the magnetic nanoparticles distributed onto the surface of the polymeric substrates. Magnetometry measurements were carried out to evaluate the magnetic behavior of these nanocomposites. Fig. 1e includes the hysteresis loops of the sample of nanoparticles (solid symbols) and of the sample of nanocomposites (hollow symbols), with values of saturation magnetization at 300 K of 51.2 and 10.1 Am^2 kg^{-1} at 300 K, respectively, because of the smaller percentage of magnetic material in the final samples [32]. The negligible values of the coercive field in both cases indicate the superparamagnetic state of the iron oxide nanoparticles, at room temperature, also reflected in the temperature-dependent ZFC-FC (zero field cooled-field cooled) magnetization curves (Fig. 1f). The average blocking temperature for these samples, as the maximum in the ZFC curve, decreases from 215 K to 147 K, as a result of the reduction in the dipolar interactions between nanoparticles in the sample of composites, due to the presence of the PS spheres [33].

3.2. Magnetic manipulation

For the magnetic manipulation to be effective, these nanocomposites are required to respond magnetically, so that they can be guided to the right location. Accordingly, we have to apply a magnetic force using an external magnetic field gradient that, in the simplest case, can overcome the hydrodynamic drag force stemming from having the nanostructures in solution [13]. In order to assess this magnetic manipulation the PS@IO nanocomposites were placed in three different media: ultrapure water (control), a glycerol/water (1:2 vol) mixture, and a cell tissue extract from mouse liver (simulating the cytosol characteristics, see the experimental section), so that the viscosity parameter playing a role is tuned. Fig. S2 in the SD includes representative confocal laser scanning microscopy (CLSM) images of the PS@IO nanocomposites in the absence (top panel) and presence of the magnetic field gradient (bottom panel), in the three different media mentioned. If no field is applied, the nanocomposites appear individually and randomly distributed. Alternatively, once the magnetic field gradient is applied, the magnetic force and torque exerted align the nanocomposites to form chains in the direction of the applied magnetic field, taking advantage of the dipolar interactions between the total magnetic moments of the composites once aligned [34]. Fig. S3 in the SD includes a photograph of the applied magnetic field set-up to obtain the CLSM images, and the graph plotting the magnetic field gradient employed in the three cases for the magnetic manipulation, decreasing exponentially with the distance *x* to the magnet position.

Depending on the medium where the PS@IO nanocomposites are dispersed, the average length of the final linear assemblies observed varies significantly, as shown in Fig. S2 (bottom panel), increasing as the viscosity of the medium considered increases. While in ultrapure water, the chains attain an average length of ∼5 µm and in the glycerol/water mixture is ∼12 µm, in the much more viscous cell tissue extract the average length is about 40–50 µm. In this regard, a high viscous medium helps the dipolar interactions between the nanocomposites to become stronger because it implies more interactions and collisions that cause them to undergo a diffusive motion which is much greater than the stan-

dard Brownian motion [35]. In this situation, the chains of n assembled nanocomposites, because of the magnetic field gradient, will reach a velocity relative to the carrier fluid defined by:

$$\Delta \upsilon = \frac{nV_{magnetic-shell}\Delta\chi}{12\pi\mu_0\eta R_c}\nabla\left(B^2\right) = \frac{\xi}{\mu_0}\nabla\left(B^2\right) \tag{1}$$

which depends on the magnetic field gradient $\nabla\left(B^2\right)$, the viscosity of the medium (η), the magnetic permeability of free space (μ_0), the geometric volume of the outer concentric magnetic shell ($V_{magnetic-shell}$), the chain hydrodynamic radius (R_C), and the magnetic susceptibility of the magnetic material in the nanocomposites relative to the carrier fluid ($\Delta\chi c$). The velocity acquired by the magnetically manipulated nanostructures is therefore linearly dependent on their 'magnetophoretic mobility' (ξ), which quantifies how magnetically manipulable they are in a particular medium, [19] and can be correlated to the medium viscosity. Accordingly, to facilitate the magnetic manipulation and to gather the dynamics information, nanostructures with a large magnetic susceptibility at low fields and in their superparamagnetic state are mandatory, jointly with a relatively large size (also easing its documentation by imaging), all characteristics fulfilled by the PS@IO nanocomposites.

The motion of the PS@IO nanocomposites was pondered in the three different media through the analysis of their dynamics in the absence and presence of the same magnetic field gradient, as summarized in Fig. 2. The different behavior stems therefore from having them dispersed in media with different known viscosity: ultrapure water (left, pale blue frame), glycerol/water mixture (center, pale green frame), and cell tissue extract (right, pale pink frame). Fig. 2a, b and c show the diffusion experiments of the PS@IO nanocomposites with no magnetic field applied, that is, the nanocomposite traces as control experiments. In these conditions, we expect the PS@IO nanocomposites to move by merely random (Brownian) motion, as it is indeed shown when having the composites in ultrapure water (Fig. 2a) or cell tissue extract (Fig. 2c). However, when it comes to the glycerol/water mixture (Fig. 2b), the graph reveals that the nanocomposites move in a specific direction (in this case in the positive *y*-axis direction) with no need for applying the external magnetic field. In this regard, we can take into account the wakes of spheres in a still environment of quiescent baths of glycerin and water mixtures that were studied, though for much larger spheres and in media with a wide range of Reynolds numbers [36]. Still, we can associate this flow of the nanocomposites shown in Fig. 2b as a result of the particular regime attained in the glycerol/water medium herein considered, by which there is a drag coefficient associated and consequently
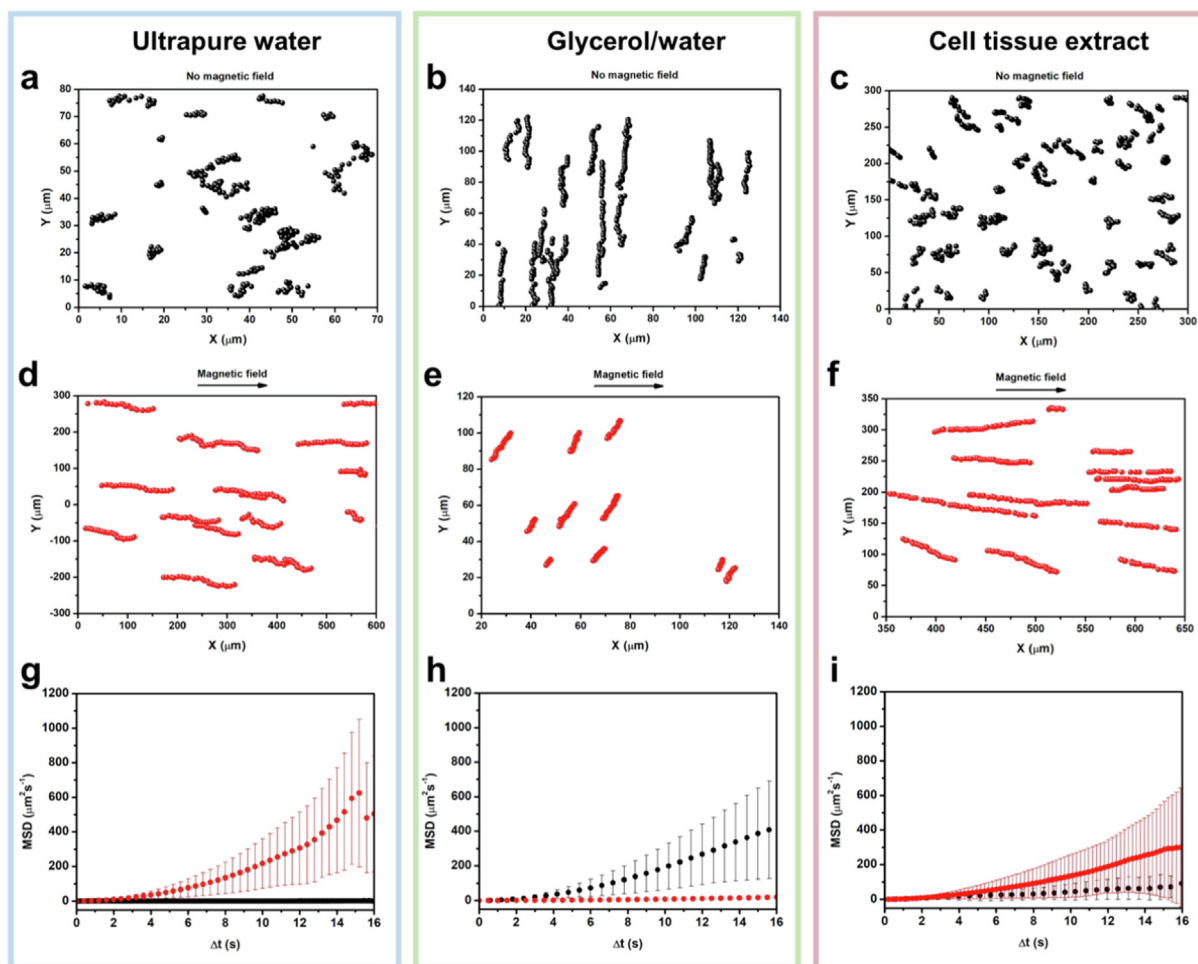
Fig. 2. Diffusion experiments in three different media: ultrapure water (a, d, g), glycerol/water mixture (b, e, h), and cell tissue extract (c, f, i). Extracted trajectories of the PS@IO nanocomposites in the absence (top, a, b, c) and the presence (center, d, e, f) of a magnetic field gradient and MSD analysis (bottom, g, h, i) of the trajectories in the absence (black) and presence (red) of the magnetic field gradient. (For interpretation of the references to colour in this figure legend, the reader is referred to the web version of this article.)

a drag force, beating the Brownian motion. Accordingly, the mobility map for the particles in this glycerol/water mixture medium reveals that Brownian motion is not governing the system, but straight trajectories are recorded (Fig. 2b).

Alternatively, when applying the magnetic force and torque because of a static magnetic field that generates a magnetic field gradient in the area of study (see Fig. S3b, in the SD), the chained nanostructures form and move cooperatively in the direction of the magnetic field (central row in Fig. 2). With the magnetic field gradient established in the positive *x*-axis direction, the magnetic force drives the motion of every magnetic nanostructure working now as microrobots in this direction, as shown in Fig. 2d and f, when dispersed in ultrapure water or the cell tissue extract, respectively. However, for the nanostructures dispersed in the glycerol/water mixture, there is a vector sum of forces, with the drag force and the magnetic force pointing in the positive *y*-axis and *x*-axis directions, respectively, with the consequent displacement taking place in the diagonal direction, as shown in Fig. 2e, which implies, therefore, a less effective magnetic manipulation.

The motion of the nanocomposites (Brownian or induced) can be analysed more quantitatively using optical tracking to obtain a mean-squared displacement (MSD) analysis [16,25]. This MSD as a function of short time intervals, in the absence (black) and presence of the magnetic field gradient (red) was acquired (bottom row in Fig. 2), so that a transition from a linear tendency (stemming from a random Brownian movement because there is no external stimulus) to a parabolic trend (induced, directed, propelled or guided movement because of some external stimulus), can be assessed [25]. For that, the MSD plots were obtained following the standard experimental protocol averaging all nanocomposites (individual or chained) present in the different movie frames, and considering no constrains in movement, except in the *z*-direction. Given the random motion of the composites in pure water and in the cell tissue extract in the absence of a magnetic field, the diffusion coefficient can therefore be calculated taking into account the motion registered by the optical tracking. Attending to the composite trajectories, since the squared displacement is linear in time (MSD = 4DΔt, *vide infra*) [25], the values of diffusion coefficient can be calculated from the slope, with values of 1.16 ($\pm$0.02) μm^2 s^{-1} and 0.43 ($\pm$0.01) μm^2 s^{-1}, in ultrapure water and the cell tissue extract, respectively. These values imply a much slower diffusive motion in the cell tissue extract, which can be associated to the larger viscosity (*vide infra*). These values are also in agreement with the Stokes-Einstein equation: $D = k_B T/6\pi\eta R$, where η is the viscosity of the medium, k_B is the Boltzmann constant, T is the temperature and R is the radius of the colloid considered.

Similarly, to evaluate the induced motion of the chains of nanocomposites due to the magnetic field as an external stimulus, the MSD analysis was evaluated. The linear to parabolic transition expected is indeed observed in Fig. 2g and i (referred to having the chains dispersed in pure water or the cell tissue extract, respectively, and under the influence of the magnetic field gradient). This is in agreement with a MSD in which both diffusion and directed movement are implied, according to:

$$MSD = 4D\Delta t + \frac{v^2\tau_r^2}{2}\left(\frac{2\Delta t}{\tau_r} + e^{-\frac{2\Delta t}{\tau_r}} - 1\right) \qquad (2)$$

which considers the random motion (first term of the equation; no external forces acting but just the movement due to thermal energy), and the induced or directed motion (quadratic term of the equation, due to the presence of an external stimulus, that is, the magnetic force in this case). For short intervals of time, Eq. (2) can be simplified to obtain Eq. (3):

$$MSD = 4D\Delta t + v^2\Delta t^2 \qquad (3)$$

as reported for the induced or directed movement, considering different types of motilities nanoparticles can undergo [16,25]. In the case of these magnetic chains, the parabolic trends observed, even at such long time delays (see MDS plots (red symbols) in Fig. 2g and i), indicate that their movement is indeed induced and guided by the external magnetic force. Consequently, a mean velocity (when applying the magnetic field) can be determined from these MSD plots, considering the average of their instantaneous velocities in every movie frame, with values of 1.56 ($\pm$0.05) μm s^{-1} and 1.05 ($\pm$0.06) μm s^{-1} in ultrapure water and cell tissue extract, respectively. These values are in agreement to the experimental ones obtained from the live tracking integrated into the tracking software (with a very similar value v = 1.47 ($\pm$0.05) μm s^{-1} and v = 1.01 ($\pm$0.05) μm s^{-1} for both experiments).

For the glycerol/water mixture, we observe the opposite behavior, with a more linear tendency in the MSD plot once the magnetic field is applied. Since for the parabolic behavior registered in the absence of magnetic field, no external stimuli were applied, other phenomena must be responsible for the non-Brownian movement registered, with different processes such as sedimentation or convective mixing currents. In the case of convective mixing, the visual inspection of the trajectories of particles would reflect this unidirectional motion of convection by straight lines at constant velocities [25], such that, all particles, over the areas visualized by optical microscopy, should move in the same direction and at the same velocity. Accordingly, since the trajectories of all the nanocomposites in the glycerol/water mixture (Fig. 2b) look indeed very similar, we can point out the convection as the dominant process moving them. At this point, it is also important to take into account that microscopic interactions in these glycerol/water mixtures are not yet well understood, particularly in fractions of glycerol <0.3–0.5, likely because inter-diffusion between solute–solute, solute–solvent, and solvent–solvent molecules may cause a non-homogeneous fluid over time [37,38]. With this into account we can postulate that when having the nanocomposites in the glycerol/water mixture, in the presence of the applied magnetic field, the formed chains move in the direction of the magnetic field, but the convective mixing makes less effective the magnetically induced and guided movement, rendering the chains much slower (see the MSD plot in Fig. 2h, red symbols and summary of dynamical values in Table 1). Still, they perceive the magnetic force and have their trajectories reoriented, demonstrating the magnetic manipulation, and anyhow, a more detailed investigation of this particular behavior is out of the scope in this report.

Both the diffusion coefficient of the nanocomposites in the absence of a magnetic field, and the magnetic manipulation of the formed chains in terms of velocity, obtained from the MSD analysis, and the magnetophoretic mobility, calculated using Eq. (1), are summarized in Table 1. From these results we can conclude that: (a) the values of diffusion of the nanocomposites are in agreement with the tabulated value of viscosity of pure water (10^{-3} Pa s) and the values of the glycerol/water mixture (2.97×10^{-3} Pa s) and the cell extract (3.18×10^{-3} Pa s), determined experimentally, [39] and (b) the chains of nanocomposites perform satisfactorily both in water and in the more viscous cell tissue extract. In this latter medium, it should be pointed out the presence of large molecules such as nucleic acids, nanometric protein aggregates (proteasomes or chaperonins), biomolecular complexes such as ribosomes, and mesometric organelles such as mitochondria, vesicles, or the centrosome, all contributing to influence the mobility of the synthetic particles. Summarizing this part, while an increase in viscosity worsens the magnetic manipulation, it also increases the final length of the chains, offering therefore a compromise between both effects in the magnetophoretic mobility, justifying the smaller value in the more viscous cell tissue extract. In the glycerol/water mixture case, even with magnetic chains twice longer than in

Table 1
Calculated values of the diffusion coefficient of the individual nanocomposites (no magnetic field applied), and of velocity (Eq. (3)) and magnetophoretic mobility (Eq. (1)), of the chained nanocomposites in the different media considered. The value* refers to HeLa cells average velocity.

Medium	Magnetic Field Gradient (mT m^{-1})	Diffusion coefficient × 10^{-6} (µm^2 s^{-1})	Velocity × 10^{-6} (m s^{-1})	Magnetophoretic Mobility × 10^{-12} (m^3 T^{-1}A^{-1}s^{-1})
Water	-	1.16	-	-
	63	-	1.56	9.0
Glycerol/Water	-	-	1.05	-
	63	-	0.26	1.5
Cell Extract	-	0.43	-	-
	63	-	1.05	6.05
Murine NIH-3T3 Cells	-	0.91	-	-
HeLa Cells	63	-	1.63*	9.4
Zebrafish yolk sac	-		0.030	-
	63	-	0.050	0.29

water, the magnetic force effect becomes poorer because of the hypothesized convective mixing, reducing significantly their final magnetophoretic mobility.

3.3. Biologically relevant media

The magnetic manipulation was assessed in vitro, in HeLa cell cultures, and *in vivo*, in zebrafish larvae. For this purpose, in the first case, the HeLa cell cultures were incubated with the serum-functionalized PS@IO nanocomposites redispersed overnight, in the absence or presence of a magnetic field gradient. In the first case, and upon internalization by receptor-mediated endocytosis and *endo*-lysosomal entrapment, the nanocomposites became gathered by the cells and displayed no apparent alignment, as shown in the representative CLSM image in Fig. 3a. As for most endocytosed nanocomposites [27], they are randomly displayed in a typically perinuclear disposition (see a more general overview in Fig. S4a, in the SD), that is, close to the blue-stained nuclei. Furthermore, the process by which the nanocomposites internalize the HeLa cells and become trapped by endocytosis was followed by TEM. Fig. S5 in the SD included images of ultra-thin sections of the nanocomposites used in the HeLa cells, showing different steps of the process called "canonical route", that is, the receptor-mediated endocytosis [40,41]. At this point, it is also worthy to note that these TEM images in Fig. S5 show healthy cells with the organelles in the cytoplasm very well preserved, revealing the very low toxicity of the nanocomposites. To study the movement of the nanocomposites within cells, and more specifically, within subcellular compartments such as endosomes, using the cytosol as reference, we have also checked the nanocomposites behavior using a flatter cell type (murine NIH-3T3 fibroblasts) that renders easier the documentation of living cells during prolonged periods using confocal microscopy, to obtain time-lapse films, for the random movement analysis. As shown in the VS1 video (included in the SD), the nanocomposites become trapped in the endosomes and if they have enough space, they move randomly. In such a situation, it is possible to estimate the dynamic viscosity of the lysosomal fluid by analysing the diffusion performance of the entrapped nanostructures. The estimated value of viscosity of 0.96 Pa·s, for the average diffusion coefficient obtained (see Table 1), is larger than other values estimated for the lysosomal viscosity of different cells (0.41 (J774A.1 (mouse macrophages)), 0.51 (BHK (baby hamster kidney fibroblasts)) and 0.73 Pa·s (HeLa cells)) [42]. In this regard, Devany et al. have associated increases

in viscosity values of this kind of organelles to an increase of storage of material, which can be also reasoned here because of the presence itself of every nanocomposite, which, as shown in the VS1 video, occupy a large percentage of the available volume of the organelle.

Alternatively, for the Hela cells incubated with the PS@IO nanocomposites in the presence of the magnetic field gradient, a few intracellular short chains of nanocomposites were observed (Fig. 3b and c, and more general overviews in Fig. S4b and c, in the SD). Since their magnetic manipulation in the cell culture implied the possibility of manipulation of the cells themselves [43,44], the HeLa cells were first detached from the glass substrate and subsequently located again under the influence of the magnetic field gradient, so that, the trajectories while pulling the cells were tracked. Since the internalization of the PS@IO nanocomposites was not homogenous in terms of an average number of nanocomposites internalized per cell, only some of the cells imaged (in pink) were displaced when manipulating at a distance the chains of nanocomposites (the trajectories appear indicated in yellow), whereas others remained still, on the substrate, as shown in Fig. 3d. An analogous MSD analysis was therefore performed for this system, as shown in Fig. 3e, offering the expected parabolic trend associated to an induced and guided movement because of the magnetic force acting as external stimulus. This parabolic function allows us to calculate the mean velocity (considering Eq. (3)), obtaining an average value of 1.63 (±0.25) µm s^{-1} for the cells imaged and showing displacement. For a clearer inspection of the movement, the inset in Fig. 3e depicts the tracking of a single cell under the influence of the magnetic field gradient, of which the average speed of the cell in this distance registered is 1.46 (±0.12) µm s^{-1}. This value is within the range of velocities obtained from the MSD analysis and slightly larger than the one obtained for the case of chains of nanocomposites navigating in ultrapure water and cell extract media. Though the chains have attained a similar length when inside the HeLa cells and under the influence of the magnetic field gradient as in ultrapure water, this velocity does not refer to their motion but to the motion of the cells. Anyway, this analysis demonstrates the effective magnetic manipulation of cells when exerting the magnetic force on these chains of nanocomposites, rendering them good candidates for cell separation applications.

Finally, we consider the zebrafish larvae to assess the manipulation of the PS@IO nanocomposites inside a living vertebrate, with optimum optical transparency that favours the experiments by
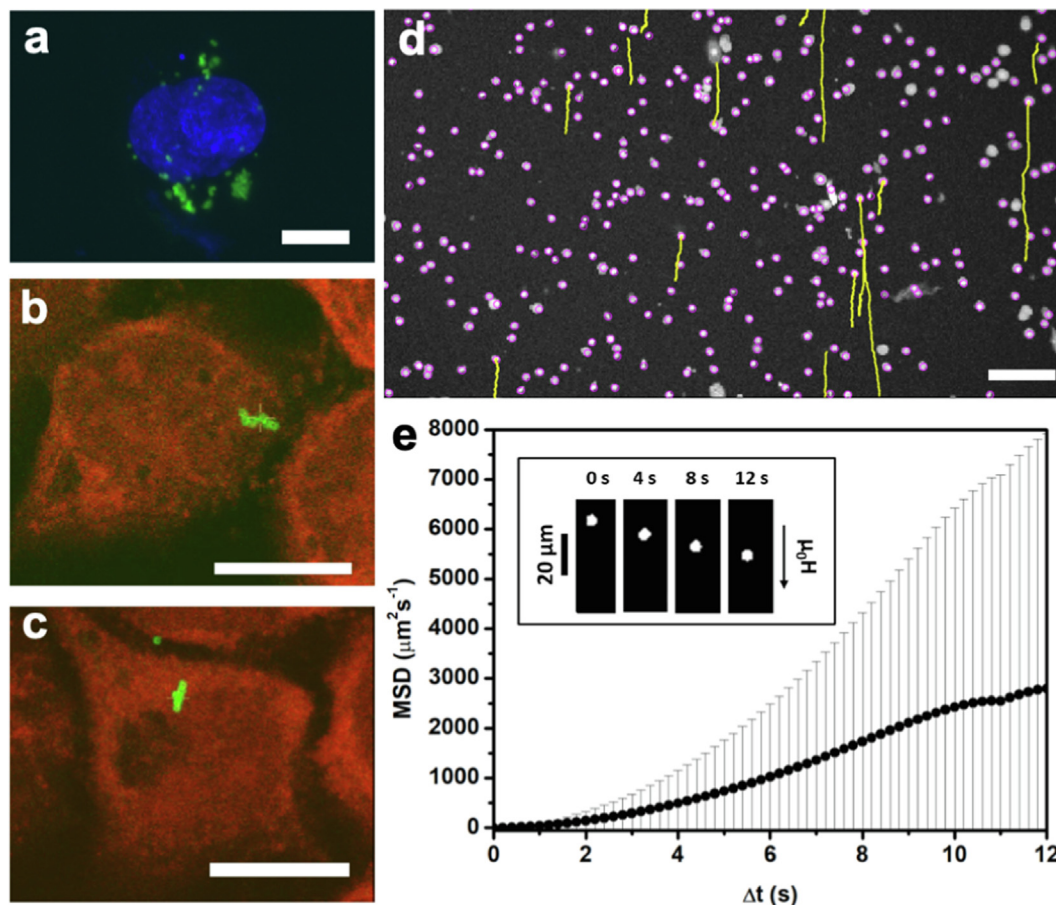
Fig. 3. CLSM projection images of HeLa cells (scale bar in a), b) and c): 10 μm). Nuclei stained with Hoechst (blue channel) displaying randomly distributed cytoplasmic PS@IO nanocomposites (green channel), in the absence of a magnetic field gradient (a). Confocal single *z*-plane images of the cytoplasm of Hela cells stained with ethidium bromide (red channel) in the presence of a magnetic field gradient, with the internalized fluorescent PS@IO nanocomposites forming magnetic chained swimmers (b and c). Whole HeLa cells (purple dots) containing intracellular chained swimmers upon the presence of an external magnetic gradient (yellow lines indicate the whole-cell trajectories in the media (scale bar: 50 μm) (d). MSD analysis of these cell ensemble trajectories (e) (inset: tracking of a single cell under the influence of the magnetic field gradient). (For interpretation of the references to colour in this figure legend, the reader is referred to the web version of this article.)

which studying the magnetophoretic mobility of the chains of nanocomposites in a highly viscous and bio-relevant environment [45,46]. Consequently, larger (3.5 μm in diameter, because of ease of imaging) PS@IO nanocomposites were similarly prepared and injected into the zebrafish yolk sac. The yolk sac is a nutrient reserve for the zebrafish embryo, separated from the rest of the embryo by the yolk syncytial layer, a multinucleate layer of cells that plays a nutritive role during embryonic and larval stages [47]. The yolk sac provides for the embryo growth during the early developmental stages with lipids, proteins, and micronutrients, and offers therefore a highly viscous medium to test both the individual nanocomposites and the chains. Additionally, either with the nanocomposites or the chains trapped in the yolk sac, both the dissemination via the vasculature and/or the binding of the nanocomposites to the endothelium can be avoided, as both effects would interfere with the magnetic manipulation experiments to be analysed. Furthermore, the initial nanocomposites were loaded with the fluorescent PAH-FITC (poly(fluorescein isothiocyanate allylamine hydrochloride)) polyelectrolyte on their surface, enabling their distribution and mobility to be easily monitored. Between 15 and 20 repeats conducted in each of four independent experiments were carried out, by which the individual or the chains of nanocomposites were let to distribute within the yolk sac, that is, in the absence or presence of a magnetic field gradient, showing the series of these four independent experiments similar

repeatability. Fig. 4 includes representative microscopy images of the zebrafish embryos, on which we can observe the cloud of injected nanocomposites, coloured in green. The images of the zebrafish in the absence (a and b) and presence (c, d) of a magnetic field gradient (represented using the magnetic field black lines included in the bottom right scheme), right after the injection (left column) and after 45 min (right column), illustrate how the nanocomposites individually or as chains become distributed. While a confined localization in both cases is attained right after the injection (Fig. 4a and c), the nanostructures distribute differently inside the yolk sac when in the absence or presence of the magnetic field gradient, that is, randomly (Fig. 4b) or with an induced motion guided in the direction of the established magnetic field gradient, after incubation of the embryos for 45 min (Fig. 4d), though with some passive diffusion contribution. Please notice that the green fluorescence seen around the yolk sac is a background signal. Fig. 4e includes the average distance distribution (travelled 45 min after the injection, by the nanocomposites, in blue, and the chains, in red), fitted to log-normal functions, such that average values of 80 (*/3) μm (in all directions) and 135 (*/2) μm (in the magnetic field gradient direction) respectively, were obtained. These average values demonstrate indeed the occurrence of an induced guided movement inside the zebrafish yolk sac. That is, when dispersed in the yolk sac, the average velocity of the nanocomposites (calculated considering these average
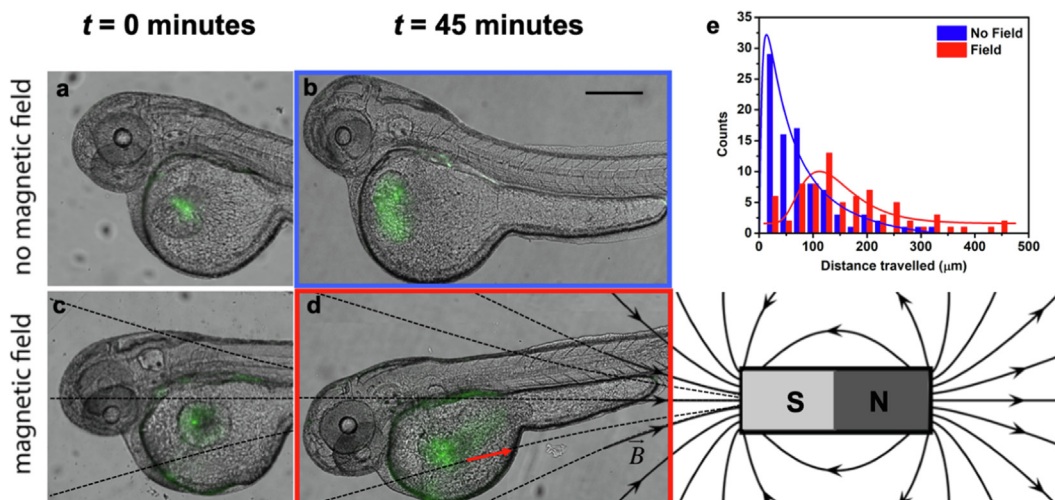
Fig. 4. Representative microscopy images (scale bar: 500 μm) of zebrafish embryos injected with PS@IO nanocomposites, right after the injection (a, c) and the same embryos incubated in the absence (b) and presence (d) of a magnetic field gradient (represented using a magnet scheme from which we can observe the magnetic field lines) after 45 min. Distance (traveled by the nanocomposites) distribution analysis (e), fitted to log-normal functions.

values of distances travelled by the nanocomposites in the 45 min period of the experiment) increases from 0.030 μm s^{-1} (in the absence of magnetic field) to 0.050 μm s^{-1} (under the influence of the magnetic field gradient, and therefore working as chains magnetically propelled). These values imply a much slower movement in both cases if compared to the other media, also taking into account the identical magnetic field gradient and even considering the larger size of the initial nanocomposites. This indicates the important role of the viscosity inside the yolk sac slowing down both the Brownian and the induced guided movement. To support this final conclusion, we have proceeded with an estimation of the viscosity of the yolk sac internal medium taking into account the average velocity under the influence of the magnetic field gradient, obtaining a rough value of ~1.26 Pa·s, that is, more than one thousand times the viscosity of pure water, which can also explain the very slow diffusion of the individual nanocomposites in the absence of the magnetic field, also taking into account the larger size of the PS spheres employed in this final case.

4. Conclusions

This work demonstrates that different biological media can be explored by magnetically propelled chained nanocomposites. The effects physical parameters like density and viscosity of the medium to be explored can exert on the chain formation and on the magnetic manipulation can indeed be correlated to the movement induced. The initial analysis of the dynamics governing the process of chain formation and magnetic manipulation in three different media (water, glycerol/water mixture and cell tissue extract) paves the way for the analysis of more complex biological media, such as the ones inside the lysosomes of cells or inside the yolk sac where nutrients to feed zebrafish embryo are loaded. In detail, the dynamics information associated to the Brownian or magnetically induced motion and obtained from optical tracking permits to estimate diffusion coefficients and velocities. These values allow the estimation of viscosity values in different biologically relevant media, offering an easier to implement method and analysis than previous strategies designed for this aim [6,42]. Further studies are under way to determine values of viscosity and modes of diffusion in other media (mucosa, blood–brain barrier, etc.), where a magnetically driven enhanced diffusion and propulsion can play a role in key applications like drug delivery.

CRediT authorship contribution statement

Miguel A. Ramos-Docampo: Methodology, Methodology, Formal analysis, Writing – review & editing. **Pablo Hurtado:** Methodology. **Ana B. Dávila-Ibáñez:** Methodology, Formal analysis, Writing – review & editing. **Roberto Piñeiro:** Methodology, Formal analysis, Writing – review & editing. **Mónica L. Fanarraga:** Methodology, Formal analysis, Writing – review & editing. **Verónica Salgueiriño:** Conceptualization, Formal analysis, Investigation, Writing – original draft, Writing – review & editing.

Declaration of Competing Interest

The authors declare that they have no known competing financial interests or personal relationships that could have appeared to influence the work reported in this paper.

Appendix A. Supplementary material

Supplementary data to this article can be found online at https://doi.org/10.1016/j.jcis.2022.08.154.

References

[1] J. Llacer-Wintle, A. Rivas-Dapena, X.-Z. Chen, E. Pellicer, B.J. Nelson, J. Puigmartí-Luis, S. Pané, Biodegradable small-scale swimmers for biomedical applications, Adv. Mater. 33 (2021) 2102049.

[2] N. Ebrahimi, C. Bi, D.J. Cappelleri, G. Ciuti, A.T. Conn, D. Faivre, N. Habibi, A. Hosovsky, V. Iacovacci, I.S.M. Khalil, V. Magdanz, S. Misra, C. Pawashe, R. Rashidifar, P.E.D. Soto-Rodríguez, Z. Fekete, A. Jafari, Magnetic actuation methods in bio/soft robotics, Adv. Func. Mater. 31 (2021) 2005137.

[3] A. van Reenen, A.M. de Jong, J.M.J. den Toonder, M.W.J. Prins, Integrated lab-on-chip biosensing systems based on magnetic particle actuation – a comprehensive revies, Lab. Chip. 2014 (1966) 14.

[4] N. Mirkhani, M.G. Christiansen, S. Schuerle, Living, self-replicating ferrofluids for fluidic transport, Adv. Func. Mater. 30 (2020) 2003912.

[5] M.A. Ramos-Docampo, M. Fernández-Medina, E. Taipaleenmäki, O. Hovorka, V. Salgueiriño, B. Städler, Microswimmers with heat delivery capacity for 3D cell spheroid penetration, ACS Nano 13 (10) (2019) 12192–12205.

[6] A. Ghosh, D. Dasgupta, M. Pal, K.I. Morozov, A.M. Leshansky, A. Ghosh, Helical nanomachines as mobile viscometers, Adv. Func. Mater. 28 (2018) 1705687.

[7] P.S. Schattling, M.A. Ramos-Docampo, V. Salgueiriño, B. Städler, Double-fueled janus swimmers with magnetotactic behavior, ACS Nano 11 (4) (2017) 3973–3983.

[8] L. Chevry, N.K. Sampathkumar, A. Cebers, J.-F. Berret, Magnetic wire-based sensors for the microrheology of complex fluids, Phys. Rev. E 88 (6) (2013), https://doi.org/10.1103/PhysRevE.88.062306.

[9] J. Yu, D. Jin, K.-F. Chan, Q. Wang, K. Yuan, L. Zhang, Active generation and magnetic actuation of microrobotic swarms in bio-fluids, Nat. Comm. 10 (2019) 5631.

[10] Q. Wang, X. Ma, H. Liao, Z. Liang, F. Li, J. Tian, D. Ling, Artificially engineered cubic iron oxide nanoparticle as a high-performance magnetic particle imaging tracer for stem cell tracking, ACS Nano 14 (2) (2020) 2053–2062.

[11] S. Martel, O. Felfoul, J.-B. Mathieu, A. Chanu, S. Tamaz, M. Mohammadi, M. Mankiewicz, N. Tabatabaei, MRI-based medical nanorobotic platform for the control of magnetic nanoparticles and flagellated bacteria for target interventions in human capillaries, Int. J. Robot. Res. 28 (9) (2009) 1169–1182.

[12] G. Kósa, P. Jakab, G. Székely, N. Hata, MRI driven magnetic microswimmers, Biomed. Microdev. 14 (1) (2012) 165–178.

[13] Q.A. Pankhurst, J. Connolly, S.K. Jones, J. Dobson, Applications of magnetic nanoparticles in biomedicine, J. Phys. D: Appl. Phys. 36 (2003) R167.

[14] J. Pokki, J. Parmar, O. Ergeneman, H. Torun, M. Guerrero, E. Pellicer, J. Sort, S. Pané, B.J. Nelson, Mobility-enhancing coating for vitreoretinal surgical devices: hydrophilic and enzymatic coatings investigated by microrheology, ACS Appl. Mater. Interf. 7 (2015) 22018.

[15] M. Fernández-Medina, M.A. Ramos-Docampo, O. Hovorka, V. Salgueiriño, B. Stadler, Adv. Func. Mater. (2020) 1908283.

[16] W. Wang, T.E. Mallouk, A practical guide to analyzing and reporting the movement of nanoscale swimmers, ACS Nano 15 (10) (2021) 15446–15460.

[17] A.D. Grief, G. Richardson, Mathematical modelling of magnetically targeted drug delivery, J. Magn. Magn. Mater. 293 (2005) 455.

[18] E. Lauga, T.R. Powers, The Hydrodynamics of swimming microorganisms, Rep. Prog. Phys. 72 (2009) 096601.

[19] M. Testa-Anta, S. Liébana-Viñas, B. Rivas-Murias, B. Rodríguez González, M. Farle, V. Salgueiriño, Shaping iron oxide nanocrystals for magnetic separation applications, Nanoscale 10 (43) (2018) 20462–20467.

[20] S. Lin, Y. Zhao, A.E. Nel, S. Lin, Zebrafish: an in vivo model for nano EHS studies, Small 9 (9–10) (2013) 1608–1618.

[21] L. Evensen, P. L. Johansen, G. Koster, K. Zhu, L. Herfindal, M. Seth, F. Fenaroli, J. hildahl, S. Bagherifam, C. Tulotta, L. Prasmickaite, G. M. Maelandsmo, E. Snaar-Jagalska, G. Griffiths, Zebrafish as a model system for chararacterization of nanoparticles against cancer, Nanoscale 8 (2016) 862.

[22] C. Zhou, E.D. Boland, P.W. Todd, T.R. Hanley, Magnetic particle characterization-magnetophoretic mobility and particle size, Cytometr. Part A. 89A (2016) 585.

[23] K.E. McCloskey, J.J. Chalmers, M. Zborowski, Magnetic cell separation: characterization of magnetophoretic mobility, Anal. Chem. 75 (2003) 6868.

[24] J. Pokki, O. Ergeneman, S. Sevim, V. Enzmann, H. Torun, B.J. Nelson, Measuring localized viscoelasticity of the vitreous body using intraocular microprobes, Biomed. Microdev. 17 (2015) 85.

[25] G. Dunderdale, S. Ebbens, P. Fairclough, J. Howse, Importance of particle tracking and calculating the mean-squared displacement in distinguishing nanopropulsion from other processes, Langmuir 28 (30) (2012) 10997–11006.

[26] R. Massart, Preparation of aqueous magnetic liquids in alkaline and acidic media, IEEE Trans. Magn. 17 (2) (1981) 1247–1248.

[27] N. Iturrioz-Rodríguez, E. González-Domínguez, E. González-Lavado, L. Marín-Caba, B. Vaz, M. Pérez-Lorenzo, M.A. Correa-Duarte, M.L. Fanarraga, A biomimetic escape strategy for cytoplasm invasion by synthetic particles, Angew. Chem. Int. Ed. 56 (2017) 13736.

[28] Eckhard Limpert, W.A. Stahel, Markus Abbt, Log-normal distributions across the sciences: keys and clues, Bioscience 51 (5) (2001) 341, https://doi.org/10.1641/0006-3568(2001)051[0341:LNDATS]2.0.CO;2.

[29] M. Testa-Anta, M.A. Ramos-Docampo, M. Comesaña-Hermo, B. Rivas-Murias, V. Salgueiriño, Raman spectroscopy to unravel the magnetic properties of iron oxide nanocrystals for bio-related applications, Nanoscale Adv. 1 (6) (2019) 2086–2103.

[30] A.M. Jubb, H.C. Allen, Vibrational spectroscopic characterization of hematite, maghemite, and magnetite thin films produced by vapor deposition, ACS Appl. Mater. Interf. 2 (10) (2010) 2804–2812.

[31] F. Caruso, M. Spasova, A. Susha, M. Giersig, R.A. Caruso, Magnetic nanocomposite particles and hollow spheres constructed by a sequential layering approach, Chem. Mater. 13 (2001) 109.

[32] M. Sanles-Sobrido, M. Bañobre-López, V. Salgueiriño, M.A. Correa-Duarte, B. Rodríguez-González, J. Rivas, L.M. Liz-Marzán, Tailoring the magnetic properties of nickel nanoshells through controlled chemical growth, J. Mater. Chem. 20 (35) (2010) 7360, https://doi.org/10.1039/c0jm01107j.

[33] S. Mourdikoudis, A. Kostopoulou, A.P. LaGrow, Magnetic nanoparticle composites: synergistic effects and applications, Adv. Sci. 8 (2021) 2004951.

[34] V. Salgueiriño-Maceira, M.A. Correa-Duarte, A. Hucht, M. Farle, One-dimensional assemblies of silica-coated cobalt nanoparticles: magnetic pearl necklaces, J. Magn. Magn. Mater. 303 (2006) 163.

[35] E. Myrovali, N. Maniotis, A. Makridis, A. Terzopoulou, V. Ntomprougkidis, K. Simeonidis, D. Sakellari, O. Kalogirou, T. Samaras, R. Salikhov, M. Spasova, M. Farle, U. Wiedwald, M. Angelakeris, Arrangement at the nanoscale: effect on magnetic particle hyperthermia, Sci. Rep. 6 (2016) 37934.

[36] J.-S. Wu, G.M. Faeth, Sphere wakes in still surroundings at intermediate reynolds numbers, AIAA J. 31 (1993) 1448.

[37] M.H. Rausch, A. Heller, A.P. Fröba, Binary diffusion coefficients of glycerol-water mixtures for temperatures from 323 to 448K by dynamic light scattering, J. Chem. Eng. Data 62 (2017) 4364.

[38] K.U. Kobayashi, R. Kurita, Ubiquitous transient stagnant domain formation during thermal convection in a well-mixed tow component fluid with large viscosity difference, Sci. Rep. 7 (2017) 12983.

[39] C.A. Sorrel, Liquid viscosity measurements using a buret, J. Chem. Educ. 48 (1971) 252.

[40] P.J. Smith, M. Giroud, H.L. Wiggins, F. Gower, J.A. Thorley, B. Stolpe, J. Mazzolini, R.J. Dyson, J.Z. Rappoport, Cellular entry of nanoparticles via serum sensitive clathrin-mediated endocytosis, and plasma membrane permeabilization, Int. J. Nanomed. 7 (2012) 2045.

[41] C. Renero-Lecuna, N. Iturrioz-Rodríguez, E. González-Lavado, E. Padín-González, E. Navarro-Palomares, L. Valdivia-Fernández, L. García-Hevia, M.L. Fanarraga, L. González-Legarreta, Effecto of size, shape and composition on the interaction of different nanomaterials with hela cells, J. Nanomater. 7518482 (2019).

[42] J. Devany, K. Chakraborty, Y. Krishnan, Subcellular nanorheology reveals lysosomal viscosity as a reporter for lysosomal storage diseases, Nano Lett. 18 (2018) 1351.

[43] K.V. Lepik, A.R. Muslimov, A.S. Timin, V.S. Sergeev, D.S. Romanyuk, I.S. Moiseev, E.V. Popova, I.L. Radchenko, A.D. Vilesov, O.V. Galibin, G.B. Sukhorukov, B.V. Afanasyev, Mesenchymal stem cell magnetization: magnetic multilayer microcapsule uptake, toxicity, impact on functional properties, and perspectives for magnetic delivery, Adv. Healthcare Mater. 5 (2016) 3182.

[44] I.V. Vidiasheva, A.A. Abalymov, M.A. Kurochkin, O.A. Mayorova, M.V. Lomova, S.V. German, D.N. Khalenkow, M.N. Zharkov, D.A. Gorin, A.G. Skirtach, V.V. Tuchin, Transfer of cells with uptaken nanocomposite, magnetite-nanoparticle functionalized capsules with electromagnetic tweezers, Biomater. Sci. 6 (2018) 2219.

[45] P.L. Johansen, F. Fenaroli, L. Evensen, G. Griffiths, G. Koster, Optical micromanipulation of nanoparticles and cells inside living zebrafish, Nat. Comm. 7 (2016) 10974.

[46] G. Pen, Y. He, X. Wang, Y. Cheng, H. Zhang, K. Savolainen, L. Mädler, S. Pokhrel, S. Lin, Redox activity and nano-bio interactions determine the skin injury potential of Co_3O_4-based Metal oxide nanoparticles toward zebrafish, ACS Nano 14 (2020) 4166.

[47] L. Carvalho, C.-P. Heisenberg, The yolk syncytial layer in early zebrafish development, Trends Cell Biol. 20 (2010) 586.